Research Article

Journal of PeptideScience

Received: 30 July 2013 Revised: 15 October 2013 Accepted: 16 October 2013 Published online in Wiley Online Library: 19 November 2013

(wileyonlinelibrary.com) DOI 10.1002/psc.2586

Mimicking hemoproteins: a new synthetic metalloenzyme based on a Fe (III)-mesoporphyrin functionalized by two helical decapeptides

Mariano Venanzi,* Sabrina Cianfanelli and Antonio Palleschi

A new metalloenzyme formed by a Fe(III)-mesoporphyrin IX functionalized by two helical decapeptides was synthesized to mimic function and structural features of a hemoprotein active site. Each decapeptide comprises six 2-aminoisobutyric acid residues, which constrain the peptide to attain a helical conformation, and three glutamic residues for improving the solubility of the catalyst in aqueous solutions. The new compound shows a marked amphiphilic character, featuring a polar outer surface and a hydrophobic inner cavity that hosts the reactants in a restrained environment where catalysis may occur. The catalytic activity of this synthetic mini-protein was tested with respect to the oxidation of L- and D-Dopa by hydrogen peroxide, showing moderate stereoselectivity. Structural information on the new catalyst and its adduct with the L- or D-Dopa substrate were obtained by the combined use of spectroscopic techniques and molecular mechanics calculations.

Additional supporting information may be found in the online version of this article at the publisher's web site.

Keywords: peptide catalyst; mini-enzyme; hemoprotein models; Dopa oxidation kinetics; helical oligopeptides; Aib

Introduction

Hemoproteins are impressive chemical machineries: A single prosthetic group, the heme, is able to promote an amazing variety of different biological functions, such as transport and storage of oxygen, transfer of electrons, oxidation of organic substrates, and destruction of peroxides [1].

The protein 3D structure controls the reactivity and specificity of the prosthetic group by tuning the geometry, number and type of metal coordination, nature of the axial ligands in the primary coordination shell, local dielectric constant, and nature of the interactions in the secondary coordination shell [2]. The environment hosting the metal ion in the reactive pocket determines the specific potential needed to start a given redox reaction and hinders the entry to the active site discriminating between competitive substrates [3].

Several model systems have been developed trying to embed the properties of a protein in a simpler molecule, with the aim to establish structure–activity relationships and understand the basic requirements that make possible to fulfill a specific function. Peptide-based compounds are intermediates between an intact large protein and a small molecular catalyst, thus being of sufficient complexity to retain the principal structural features of a protein environment and simple enough to improve the comprehension of the factors determining the reactivity of natural systems.

Several excellent review articles, collecting seminal results in the field, have appeared in the literature, to which the interested reader can refer for a detailed description of the history of peptide models of heme proteins [4]. Shortly, they can be classified in two broad families: models in which (i) the peptide chains are covalently linked to the porphyrin scaffold or (ii) self-assemble around the porphyrin site by exploiting noncovalent interactions. Among the former, the field was pioneered by the introduction of microperoxidases, heme–peptide fragments obtained by the proteolytic digestion of cytochrome c [5], and the monopeptide–deuteroheme complex of Casella and co-workers [6]. This work culminated in the paradigmatic four-helix bundle model developed by DeGrado and co-workers [7], which, besides fundamental acquisition on the understanding of protein folding and function, leads to a wide range of applications from catalysis [8] to biosensing [9], paving the way for the fast-growing field of bio-inspired nanotechnology [10].

At an intermediate level of complexity between simple porphyrin derivatives and isolated protein fragments, Pavone and co-workers [11] and Benson and co-workers [12] developed a helix–heme–helix sandwich model composed of two helical peptides covalently linked through the amino group of a Lys side chain to the twin propionates of deuteroporphyrin IX and mesoporphyrin II or IX, respectively.

* *Correspondence to: Mariano Venanzi, Department of Chemical Sciences and Technologies, University of Rome Tor Vergata, Via della Ricerca Scientifica 1, 00133 Rome, Italy. E-mail: venanzi@uniroma2.it*

Department of Chemical Sciences and Technologies, University of Rome Tor Vergata, Rome, Italy

Abbreviations: *10Np, H-Ala-Aib-Glu(OtBu)-Aib-Glu(OtBu)-(Aib)$_3$-Glu(OtBu)-Aib-OCH$_2$-CH$_2$-Napht; mP(10N)$_2$, mesoporphyrin IX/(Ala-Aib-Glu-Aib-Glu-(Aib)$_3$-Glu-Aib-OCH$_2$-CH$_2$-Napht)$_2$ conjugate; FemP(10N)$_2$, Fe(III)-mesoporphyrin IX/(Ala-Aib-Glu-Aib-Glu-(Aib)$_3$-Glu-Aib-OCH$_2$-CH$_2$-Napht)$_2$ conjugate.*

Journal of PeptideScience

In their peptide models of hemoprotein, one or two His residues were suitably inserted in the peptide chain to coordinate the central iron ion, giving rise to pentacoordinated high-spin species in the monoadducts and hexacoordinated low-spin systems in the bis-adducts. Interestingly, the molecule showing the highest content of pentacoordinated structures also showed the highest activity, suggesting that a tight binding of the protein environment in peptide–heme adducts or bis-histidine coordination in peptide-sandwiched porphyrins prevents the heme from reacting with an exogenous ligand.

We report here on a new synthetic catalyst also based on the peptide–heme–peptide motif, composed of a Fe(III)-mesoporphyrin IX covalently linked to two amphiphilic helical decapeptides. The new compound is characterized by a polar outer surface and a hydrophobic inner cavity, which could host the reactants in a restrained catalytic environment. The idea is to have a peptide catalyst soluble in water, sufficiently protected against oxidative degradation, and capable of chiral discrimination.

The molecular formula of the investigated compound, denoted in the following as FemP(10N)$_2$, is shown in Figure 1. It embodies a Fe(III)-mesoporphyrin IX, the propionyl sites of which were covalently linked to the *N*-terminal Ala residues of two identical decapeptides (10N). The presence of six α-aminoisobutyric acid (Aib) residues constrains the two peptide chains to attain a helical conformation, because of the steric hindrance exerted by the *gem*-dimethyl substitution on the Aib C$^{\alpha}$ atom [13]. Three Glu residues were also included (at positions 3, 5, and 9) in the peptide chain for improving the solubility of the catalyst in aqueous solutions, giving rise to the formation of an amphiphilic helix. Mesoporphyrin IX was used instead of protoporphyrin IX, because the former, lacking the two ring-substituent vinyl groups, is less sensitive to the attack of oxidants, thus improving the catalyst resistance [12]. Furthermore, the two peptide chains were each *C*-terminally derivatized as naphthyl esters to obtain structural information from fluorescence energy transfer (FRET) measurements [14].

The Glu residues play a key role in mimicking the hemoprotein activity for both structural and reactivity reasons. From the structural point of view, the Glu carboxyl groups could coordinate the central iron atom, stabilizing a specific conformation. Furthermore, the protonation of the Glu side chains can be suitably varied, modulating the local polarity of the active site environment and, hence, its redox potential and reactivity. Recently, it was shown that carboxyl groups can exert a distal effect on the active site reactivity in peroxidases, opening electron transfer pathways

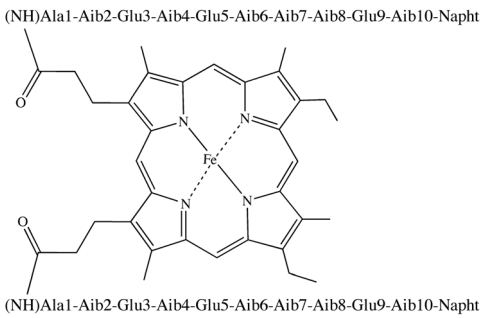

FemP(10N)$_2$

Figure 1. Molecular formula and acronym of the synthesized peptide–heme–peptide compound. *O*-Napht denotes a 2-(1-naphthyl)ethyl ester group by which the two decapeptides are *C*-terminally derivatized.

to the porphyrin macrocycle through the heme propionates [15]. This is particularly relevant in view of the choice of not inserting His residues in the peptide chains of the newly designed catalyst. In natural hemoproteins, histidines strongly coordinate the Fe(III) ion, and for this reason, they were generally introduced in most of the peptide models described so far in the literature. An issue of concern in this contribution is the capacity of peptide-based catalysts lacking His residues to mimic the activity of hemoproteins and protecting the active site from oxidative degradation, but still preserving its functionality.

Materials and Methods

Synthesis

The synthesis of the side chain-protected decapeptide H-Ala-Aib-Glu(OtBu)-Aib-Glu(OtBu)-(Aib)$_3$-Glu(OtBu)-Aib-OCH$_2$-CH$_2$-Napht (10Np) was performed by classical methods in solution via fragment condensations following strategies previously elaborated for Aib peptides [16]. At first, the Z-Aib-OH was esterified with 2-(2-naphthyl)ethanol by 1-ethyl-3-(3-dimethylaminopropyl) carbodiimide hydrochloride (EDC·HCl) in the presence of DMAP. *N*-terminal elongation of this ester to the decapeptide derivative was performed in stepwise manner by intermediate N^{α}-hydrogenolytic removal of the Z protecting group and acylation with the related Z-Glu(OtBu)-OH and Z-Aib-OH derivatives via hydroxybenzotriazole(HOBt)/EDC·HCl and 1-hydroxy-7-azabenzotriazole(HOAt)/EDC·HCl, respectively, and finally with Z-Ala-OH via HOBt/EDC·HCl. In the final step, mesoporphyrin IX and Fe(III)-mesoporphyrin IX were solubilized in CH_2Cl_2 and reacted with H-Ala-Aib-Glu(OtBu)-Aib-Glu(OtBu)-Aib-Aib-Aib-Glu(OtBu)-Aib-OCH$_2$-CH$_2$-Napht, respectively, which was obtained by catalytic hydrogenation (Pd/C in CH_3OH) of the corresponding Z derivative, and *N*-methylmorpholine. The still protected mesoporphyrin IX and Fe(III)-mesoporphyrin IX conjugates were purified by flash chromatography on silica gel using CH_2Cl_2/EtOH (9.2 : 0.8) and CH_2Cl_2/EtOH/AcOH (8.9 : 0.65 : 0.45) as eluent, respectively. Final deprotection of the two conjugates was achieved by exposure to TFA/CH_2Cl_2 (1 : 1) for 3 h. The desired mesoporphyrin IX and Fe(III)-mesoporphyrin IX constructs were obtained as well as characterized compounds after HPLC using a semi-preparative reversed phase column (Supelco, Bellefonte, Pennsylvania) and as eluent CH_3CN/H_2O/TFA (75 : 25 : 5) and monitoring the absorption of the product at $\lambda = 226$ nm. Final and intermediate products were characterized by melting point determination, TLC, rotatory optical power, IR absorption, mass spectrometry, and ^{1}H-NMR. Details on the synthetic procedures and characterization of intermediates and products are provided in Supporting Information.

Methods

TLC was carried out on silica gel (60F254, Merck Italy, Vimodrone, Italy) using five different eluents: chloroform/ethanol 9 : 1 (Rf_1), n-butanol/AcOH/H_2O 3 : 1 : 1 (Rf_2), toluene/ethanol 7 : 1 (Rf_3), AcOEt/petroleum ether 1 : 3 (Rf_4), and AcOEt/petroleum ether 1 : 1 (Rf_5). Flash chromatography was carried out using silica gel as stationary phase. HPLC purifications were carried out by a Hewlett-Packard A7554 (Agilent Technologies, Santa Barbara, CA, USA) with UV detection at $\lambda = 226$ nm using a semi-preparative reverse-phase column (Supelco LC-18-DB, $l = 25$ cm, $d = 10$ mm, Bellefonte, Pennsylvania). CD measurements were carried out by a JASCO

J600 spectropolarimeter (Jasco Europe, Cremella, Italy), by using quartz cells ($l = 0.1$, 0.5, and 1 cm). CD spectra are reported as molar ellipticity per residue (θ, degree cm^2 dmol^{-1}). Steady-state and time-resolved fluorescence experiments were performed on the same apparatus (CD900, Edinburgh Analytical Instruments, UK) by using a Xe lamp (450 W) for spectral measurements (analog detection) or a pulsed arc lamp (30 kHz repetition rate) for time decays measurements (single photon counting detection). The arc lamp was filled with ultrapure hydrogen (pressure 0.4 atm) for exciting the sample in the UV ($\lambda = 280$ nm). Under these conditions, the full width at half maximum of the excitation pulse was 1.1 ns. Time decays were analyzed through iterative reconvolution of a multiexponential function by using standard software supplied by Edinburgh Analytical Instruments (Edinburgh, UK). All solutions were freshly prepared and fluxed for 20 min in ultrapure N_2 to minimize oxygen quenching effects. Polarimetric measurements were carried out on a Perkin-Elmer polarimeter (PE-241, Waltham, MA, USA). Temperature ($T = 25$ °C) was controlled by a Haake D8 thermostat (Vreden, Germany). FAB- and ESI-mass spectra were obtained with a Sciex API-365 mass spectrometer (Perkin-Elmer, Waltham, MA, USA) equipped with a triple quadrupole ESI-MS. Fourier transformed infrared (FTIR) spectra were obtained with a PE 1720 FTIR spectrometer (Perkin-Elmer, Waltham, MA, USA) by using CaF_2 cells (optical length = 0.01, 0.1, 1 cm). ^{1}H-NMR experiments were carried out with a Bruker AM400 NMR spectrometer (Billerica, MA, USA). Chemical shifts were expressed as parts per million with respect to tetramethylsilane. 2D-NMR experiments were processed by the UXNMR code from Bruker. UV–vis absorption measurements were recorded on a thermostated JASCO 7850 (Jasco Europe, Cremella, Italy), using quartz cells (0.5 and 1 cm). Kinetic experiments were performed on the same apparatus for nine different substrate concentrations in the range between 8.0 10^{-6} and 2.9 10^{-4} M. The enzyme concentration was kept constant at 8.5 10^{-6} M, while the H_2O_2 oxidant concentration was 1.5 10^{-4} M. Each kinetic experiment was repeated in triple (pH = 7.5, $T = 25$ °C). Molecular mechanics calculations were carried out by using homemade programs, exploiting the MM4 force field [17,18]. The following procedure was adopted: (i) The two peptide backbones were initially considered in an ordered helical conformation, exploring both 3_{10}- and α-helical structures. The conformers arising from internal rotation around the torsional angles of the side chains linking the porphyrin and naphthyl chromophores were built up by making use of the rotational isomeric state model. (ii) The conformational energy was then optimized by varying all torsional angles associated to both the peptide backbones and the side chains; (iii) the Glu side chain carboxyl groups were considered in both neutral and anionic (carboxylate) forms.

Assumption (i) strongly reduced the computational effort and is based on the CD and NMR experimental evidences on the secondary structure attained by the two decapeptide chains. The potential energy comprised electrostatic, nonbonding, hydrogen bond, and torsional interactions and was calculated by using standard bond angles and lengths for both the backbone and the side chains, as implemented in the MM4 force field [18]. Coulombic interactions were assessed by assigning partial atomic charges to all atoms. Energy minimization refinement was performed by relaxing the fixed geometry for all the internal degrees of freedom and introducing stretching and bending terms. Solvent effects were taken into account by assuming a distance-dependent dielectric constant [$\varepsilon(R_{ik})$], where R_{ik} is the distance between the i and k atoms.

Results and Discussion

Spectroscopic Results

FTIR absorption

Helical peptides feature characteristic IR absorption in the 3420–3310 cm^{-1} range, associated to the stretching of NH amide groups, and between 1720 and 1660 cm^{-1} (stretching of CO amide groups) [19]. The onset of secondary structure, promoted by formation of intramolecular hydrogen bonds, can be easily observed by the progressive shift to lower energies of the NH and CO stretching frequencies with increased length of the peptide chain from two to ten residues during the synthesis of the protected decapeptide Z-Ala-Aib-Glu(OtBu)-Aib-Glu(OtBu)-(Aib)$_3$-Glu(OtBu)-Aib-OCH$_2$-CH$_2$-Napht (10Np) (Figures S1 and S2 of Supporting Information). The FTIR spectrum of FemP(10N)$_2$ in $CDCl_3$, reported in Figure 2, shows a very weak absorbance at $\bar{\nu} = 3435$–3425 cm^{-1}, ascribable to free NH groups, and a predominant absorption band peaked at $\bar{\nu} = 3325$ cm^{-1}, assigned to hydrogen-bonded NH's [19]. The intramolecular character of the hydrogen bonding interaction was confirmed by concentration-dependent FTIR absorption measurements from 0.1 to 10 mM.

The ratio between the number of NH protons involved in hydrogen bond formation (n_b) and the number of free NH's (n_f) can be estimated from the areas of the two corresponding IR absorption bands and the associated molar extinction coefficients ε_b and ε_f, that is,

$$\frac{n_b}{n_f} = \frac{A_b}{A_f} \cdot \frac{\varepsilon_f}{\varepsilon_b} \quad (1)$$

The $\varepsilon_b/\varepsilon_f$ ratio was determined by us through extensive IR measurements on several conformationally constrained oligopeptides attaining a 3_{10}-helix conformation [19]. Deconvoluting the IR spectrum reported in Figure 2, we obtained $n_b/n_f = 2.7$, a value intermediate between those expected for a pure α-helix (2.3) and a 3_{10}-helix structure (4) [20].

1H-NMR

By TOCSY and ROESY experiments in $CDCl_3$, we were able to identify the amide protons of Ala1 and Aib2 and of two Glu

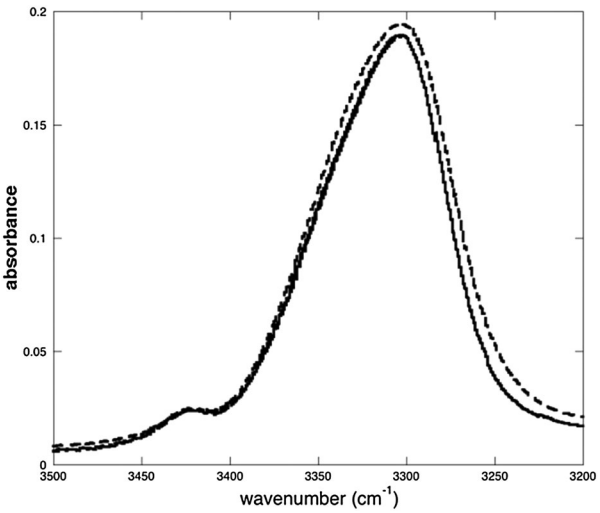

Figure 2. FTIR absorption spectra of FemP(10N)$_2$ in $CDCl_3$ in the NH absorption region [1 mM (dashed); 0.1 mM (continuous)].

Journal of PeptideScience

and one Aib residues of 10Np. It was not possible to identify the other amide protons because of the extensive overlap between the naphthyl and Z group's resonances. Titration experiments with DMSO-d_6 allowed us to have a clear indication on the conformational properties of this decapeptide derivative, because only the resonance frequencies of protons not involved in hydrogen bonding are affected (downshifted) by DMSO, a strong hydrogen bond acceptor. In Figure 3, we reported the effects of the DMSO titration on the NMR signals of the 10Np protons identified by 2D-NMR experiments. As can be seen, only the Ala1 and Aib2 protons were seriously perturbed by adding DMSO, suggesting that the protected decapeptide in $CDCl_3$ predominantly populates a 3_{10}-helix structure characterized by an $i \leftarrow i+3$ hydrogen bond network.

CD

CD measurements in CH_3OH confirmed that 10Np predominantly attains a helically ordered conformation also in this solvent, showing well-defined dichroic negative maxima at $\lambda = 207$ ($\pi \rightarrow \pi^*$ amide transition) and 226 nm ($n \rightarrow \pi^*$ amide transition). Very similar CD spectra were obtained for mP$(10N)_2$ and FemP $(10N)_2$ in the same solvent (Figure 4), the ratio between the CD molar ellipticities at $\lambda = 208$ and 227 nm, that is,

$$R = \frac{\theta(227)}{\theta(208)} \qquad (2)$$

being 0.71, 0.75, and 0.79 for 10Np, mP$(10N)_2$ and FemP$(10N)_2$, respectively. *R* values in the range 0.15–0.40 are considered diagnostic of the 3_{10}-helical conformation, while values close to 1 were found to be typical of the α-helix [21]. These results, in agreement with the FTIR data, indicate the predominant population of helical structures in both apolar ($CDCl_3$) and polar (CH_3OH) solvents, probably in equilibrium between 3_{10}- and α-helical conformations. The close similarity between the mP$(10N)_2$ and FemP $(10N)_2$ CD curves suggests that in CH_3OH, only a weak interaction between the Fe(III) central ion and the carboxylic side chain of the Glu residues is established. The relatively low intensity of the obtained CD spectra can be ascribed to the presence of six

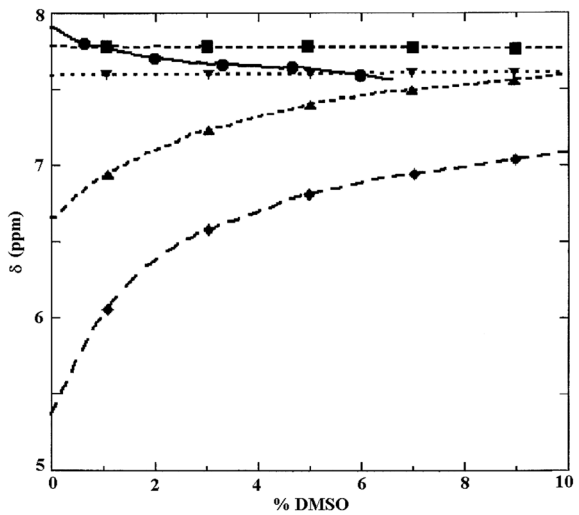

Figure 3. DMSO titration in $CDCl_3$ of the NMR signals of the protected decapeptide 10Np protons identified by 2D-NMR experiments. (♦)Ala1; (▲)Aib2; (▼) Aib; (●) Glu; (■)Glu.

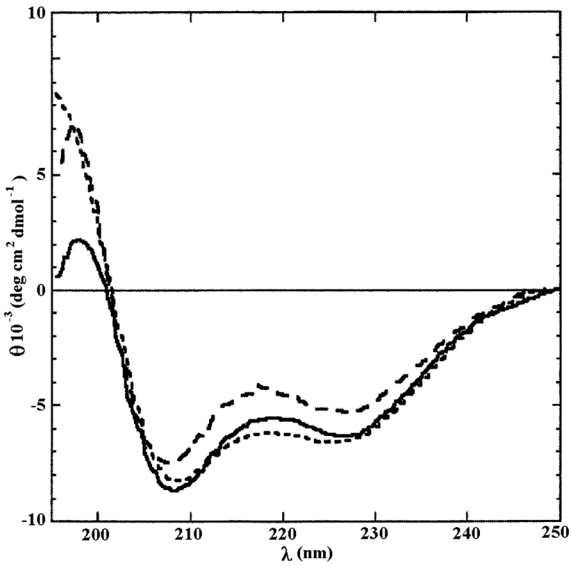

Figure 4. CD spectra of 10Np(dashed), mP$(10N)_2$ (continuous), and FemP$(10N)_2$ (dotted) in CH_3OH. Peptide concentration is 0.1 mM in all cases.

achiral residues in the peptide chain (CD ellipticities are normalized per residue molar concentration) [22].

Interestingly, the CD spectra of FemP$(10N)_2$ in H_2O/CH_3OH (9 : 1, v/v) solutions at pH 4 and pH 7.5, reported in Figure 5, reveal a strong pH dependence of the CD curves, the *R* ratio being 0.90 at pH 4 and 0.48 at pH 7.5, respectively. These results suggest that an $\alpha \rightarrow 3_{10}$-helix transition on going from pH 4 to pH 7.5 takes place. This conformational transition could be promoted by either the repulsive interaction between the deprotonated Glu carboxylates at pH 7.5 [pK_a(Glu) = 4.1] or the coordination of the Fe(III) ion to the Glu carboxyl groups of the two peptide chains.

However, the CD spectrum of the free-base compound mP $(10N)_2$ in H_2O/CH_3OH (9 : 1, v/v) at pH 7.5 shows an *R* value equal to 0.81, suggesting that the Fe(III)–COO^- interaction is mainly responsible for the conformational transition observed in the case of FemP$(10N)_2$ (Supporting Information).

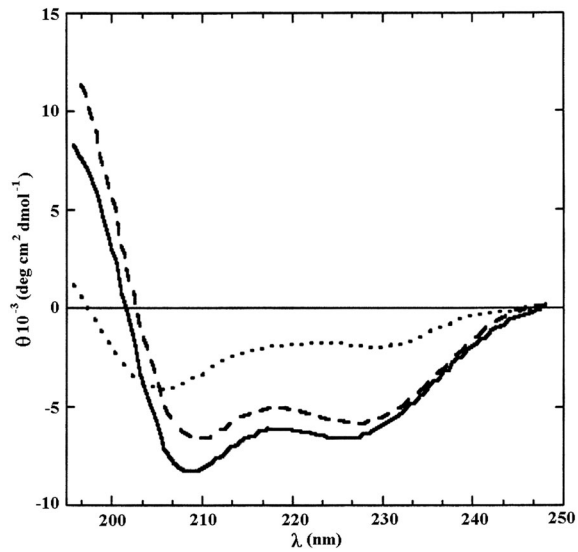

Figure 5. CD spectra of FemP$(10N)_2$ in CH_3OH (continuous) and in H_2O/CH_3OH (9 : 1, v/v) at pH 4 (dashed) and pH 7.5 (dotted). Peptide concentration is 0.1 mM in all cases.

UV–vis absorption

UV–vis absorption spectroscopy may provide relevant information on the structural features of the hemoprotein active site, because the characteristic absorption spectrum of iron porphyrins depends on the symmetry and strength of metal coordination, spin, and oxidation state [23]. The UV–vis absorption features in CH_3OH of both $FemP(10N)_2$ and $mP(10N)_2$ are reported in Table 1. As it is well known, the insertion of a metal ion strongly perturbs the absorption features of free-base porphyrins in both the Soret ($\lambda = 400$ nm, $S_0 \rightarrow S_2$) and the Q bands ($\lambda = 450$–650 nm, $S_0 \rightarrow S_1$) regions. The $mP(10N)_2$ absorption spectrum shows the two UV absorption bands typical of the naphthyl chromophores ($\lambda = 222$ and 280 nm), the very intense Soret transition peaked at $\lambda = 395$ nm, and the four Q bands system in the visible region, characteristic of free-base porphyrins. The insertion of the metal ion shifts the Soret transition to shorter wavelengths ($\lambda_{max} = 392$ nm), sensibly decreases its intensity, and gives rise to a shoulder at lower wavelengths ($\lambda = 345$ nm, sh), typical of high-spin Fe(III). Major perturbations can be observed in the visible region where the Q bands collapse to a two-band system, because of the D_{4h} symmetry of Fe(III) coordination to the porphyrin *N*-ligands. Interestingly, in H_2O/CH_3OH $(9:1)_{v/v}$ at pH 7.5, the shoulder at $\lambda = 345$ nm markedly increases, and the Q bands sensibly shift to lower energies, suggesting a stronger coordination of Fe(III) to the Glu3 carboxylate side chain groups. It should be noted, however, that the spectral features of the metalated porphyrin indicate that, in this environment, the iron center is in a high-spin state, suggesting that either a single carboxylic group is coordinating the metal ion or a weak bis-coordination of the two Glu3 carboxyl groups takes place at relatively large distances.

Fluorescence measurements

The presence of naphthalene and porphyrin chromophores, a well-known energy transfer donor–acceptor (D–A) pair, allowed us to apply Förster resonance energy transfer (FRET) to obtain structural information on the conformations attained in solution by the compounds investigated [14,24].

In Figure 6, we reported the fluorescence spectra of 10Np, $mP(10N)_2$, and $FemP(10N)_2$ in CH_3OH obtained by excitation at $\lambda = 280$ nm and dominated by the emission of the naphthyl fluorophore. From the figure, the quenching of the naphthalene emission caused by $N^* \rightarrow$ mP or $N^* \rightarrow$ FemP transfer of excitation energy can be readily observed. The FRET quenching efficiency was obtained by measuring the naphthyl quantum yield in $FemP(10N)_2$ and $mP(10N)_2$ with respect to the protected decapeptide assumed as reference compound, that is,

$$E_N = 1 - \frac{\Phi_N[\text{FemP}(10\text{N})_2 \text{ or } \text{mP}(10\text{N})_2]}{\Phi_N(10\text{Np})} \quad (3)$$

From steady-state fluorescence measurements, we obtained $E_N = 0.86$ and 0.91 for $mP(10N)_2$ and $FemP(10N)_2$, respectively.

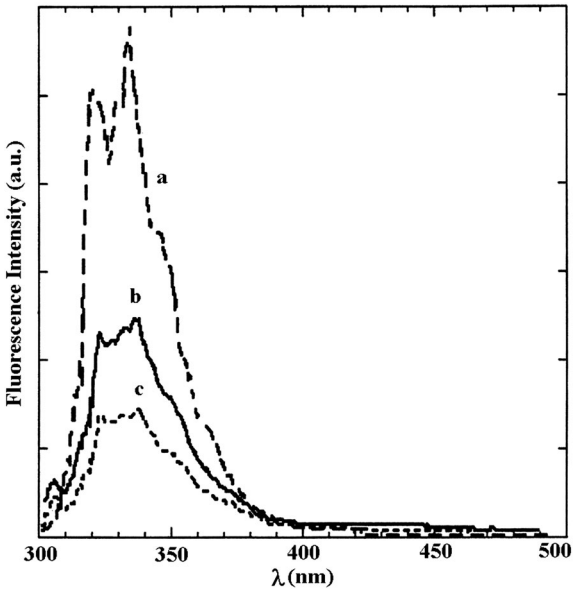

Figure 6. Fluorescence spectra of 10Np (a, dashed), $mP(10N)_2$ (b, continuous), and $FemP(10N)_2$ (c, dotted) in CH_3OH. The emission bands of $mP(10N)_2$ and $FemP(10N)_2$ were magnified by a factor 4 for clarity ($\lambda_{exc} = 280$ nm).

Energy transfer efficiencies can be also measured by evaluating the enhanced fluorescence emission of the acceptor moiety caused by energy transfer from the donor group [25]. In the present case, however, this can be carried out for the free-base porphyrin compound only, because of total quenching of the porphyrin emission caused by Fe(III) in $FemP(10N)_2$. The energy transfer efficiency, calculated from the enhanced fluorescence intensity of $mP(10N)_2$ ($E_P = 0.85$), indicates that energy transfer is the only quenching mechanism affecting the relaxation of the excited naphthyl chromophores in this compound.

In favorable conditions, time-resolved fluorescence experiments may give detailed information on the conformations populated by the molecules and their different contributions to the overall quenching process. This is because FRET quenching efficiency depends on the distance and orientation between the D–A pairs and, hence, it is the characteristic of the specific conformation attained by a macromolecule [26].

Fluorescence time decays are usually described by a sum of exponential time components, that is,

$$I(t) = \sum_{i=1}^{n} \alpha_i \exp\left(-\frac{t}{\tau_i}\right) \quad (4)$$

where α_i is the weight associated to the lifetime τ_i. Provided that the different conformers do not interconvert in the nanosecond time scale, so that dynamical averaging of the instantaneous relative positions of the donor and acceptor pair cannot take place, each decay time component can be associated to a specific

Table 1. UV–vis absorption features of $FemP(10N)_2$ and $mP(10N)_2$ in CH_3OH

Sample	λ_{max} (nm) (ε, $M^{-1}\,cm^{-1}$)	λ_{max} (nm) (ε, $M^{-1}\,cm^{-1}$)	λ_{max} (nm) (ε, $M^{-1}\,cm^{-1}$)	λ_{max} (nm) (ε, $M^{-1}\,cm^{-1}$)
$mP(10N)_2$	222 (70 000)	280 (6100)	395 (125 000)	
Q bands	499 (17 800)	530 (13 400)	568 (9600)	618 (6400)
$FemP(10N)_2$	222 (70 000)	280 (6100)	345 (sh)	392 (110 000)
Q bands	483 (13 000)	590 (10 000)		

Journal of PeptideScience

conformer. Furthermore, in the absence of ground-state interactions, the experimental pre-exponential factors α_i can be directly associated to the Boltzmann-weighted populations of each conformer [26].

The emission time decay of the naphthyl groups in FemP(10N)$_2$ and mP(10N)$_2$ is described by a three-exponential function, the decay parameters of which are reported in Table 2. From these values, it is possible to define an average time decay, that is,

$$< \tau >= \frac{\sum_i \alpha_i \tau_i}{\sum_i \alpha_i} \quad (5)$$

also reported in Table 2. The experimental quenching efficiencies associated to the *i*-th time component of the mP(10N)$_2$ and FemP(10N)$_2$ time decays can be obtained from the simple equation:

$$E_i = 1 - \frac{\tau_i}{\tau_0} \quad (6)$$

where τ_0 is the lifetime of the naphthyl fluorophore in absence of the porphyrin quencher, measured from the 10Np time decay in CH_3OH ($\tau_0 = 52.5$ ns) and in H_2O/CH_3OH (9 : 1)$_{v/v}$ at pH 7.5 ($\tau_0 = 36.2$ ns), respectively. From the average time decay $< \tau >$, an average quenching efficiency, which can be directly compared with the static quenching efficiency [Eqn 3], can be introduced. The quenching efficiencies obtained for mP(10N)$_2$ and FemP(10N)$_2$ in CH_3OH and H_2O/CH_3OH (9 : 1)$_{v/v}$ are reported in Table 3.

In structural terms, the energy transfer efficiency can be accounted for by the Förster dipole–dipole model:

$$E_i = \left\{ 1 + \frac{2}{3k_i^2} \cdot \left(\frac{R_i}{R_0} \right)^6 \right\}^{-1} \quad (7)$$

where R_i is the center-to-center distance of the D–A pair in the *i*-th conformer and k_i a dimensionless geometric factor determined by the D–A relative orientation in space [27]. R_0 is a pure spectroscopic parameter characteristic of the D–A pair, representing the distance at which 50% transfer of excitation energy occurs. For the naphthyl–FemP pair, $R_0 = 38.0$ Å in CH_3OH and 32.9 Å in H_2O/CH_3OH (9 : 1)$_{v/v}$. The data reported in Table 3 reveal that, for both the compounds investigated, almost all the populated conformers (98–99%, from the sum of α_1 and α_2 in Table 2) are characterized by a very high quenching efficiency. Although these results are mainly determined by the large R_0 values of the naphthyl–FemP pair, they strongly suggest that FemP(10N)$_2$ attains compact 3D structures in both the CH_3OH and H_2O/CH_3OH environments. In particular, analyzing the short-time components of the naphthyl time decay in the different compounds, it appears that the FemP(10N)$_2$ time decay in CH_3OH is almost similar to that measured for mP(10N)$_2$ in the same solvent, in nice agreement with CD results. On the contrary, the naphthyl time decay of FemP(10N)$_2$ in H_2O/CH_3OH 9 : 1 (v/v) at pH = 7.5 is accounted for by definitely shorter lifetimes (Table 2), suggesting that the naphthyl–FemP pair is located at short distances. Conformational energy calculations were therefore carried out to substantiate this finding.

Conformational Analysis of FemP(10N)$_2$

The conformational properties of FemP(10N)$_2$ were investigated by molecular mechanics calculations, exploring both 3_{10}- and α-helical structures and considering the Glu side chain carboxyl groups in both neutral and anionic (carboxylate) forms.

The most stable structures of FemP(10N)$_2$ in H_2O/CH_3OH (9 : 1)$_{v/v}$ at pH 4 and pH 7.5 are reported in Figure 7A and 7B, respectively. In the minimum energy structure at pH 4, the closest Fe–O (COOH) distance is 3.58 Å, suggesting that only a very weak interaction between the Fe(III) ion and the two Glu3 carboxylic oxygen atoms takes place, in good agreement with spectroscopic results. As a consequence, the helical peptide chains are dynamically free to attain the most stable α-helix conformation. On the other hand, at pH 7.5, electrostatic interactions favor the apical coordination of the two Glu3 carboxylate groups to the central metal ion causing a severe distortion of the peptide backbone (Fe–O minimal distance = 2.59 Å). Interestingly, the Fe(III)–(Glu3) carboxylate interaction constrains the *N*-terminal peptide segment to attain a β turn-like structure that closely reproduces the onset of a 3_{10}-helix conformation. This finding parallels the CD results, suggesting an α-helix to a partial 3_{10}-helix transition on going from pH 4 to pH 7.5. It should be noted, however, that the Fe(III)–O(Glu3) distances are relatively large with respect to the distances (~2 Å) attained by the strongly coordinated iron

Table 2. Time decay parameters for mP(10N)$_2$ and FemP(10N)$_2$ in CH_3OH and 9 : 1 (v/v) H_2O/CH_3OH solution[a]

Sample	α_1	τ_1/ns	α_2	τ_2/ns	α_3	τ_3/ns	$< \tau >$/ns
mP(10N)$_2$	0.58	1.6	0.40	4.7	0.02	35.2	3.5
FemP(10N)$_2$ (CH_3OH)	0.65	1.6	0.34	4.2	0.01	34.6	2.8
FemP(10N)$_2$ H_2O/CH_3OH 9 : 1 (v/v) pH = 7.5	0.74	0.9	0.24	3.8	0.02	36.2	2.3

[a] $T = 25$ °C, $\lambda_{exc} = 280$ nm, and $\lambda_{em} = 340$ nm.

Table 3. Experimental quenching efficiencies of mP(10N)$_2$ and FemP(10N)$_2$ in CH_3OH and H_2O/ CH_3O H (9 : 1)$_{v/v}$

Sample	E_1[a]	E_2[a]	E_3[a]	$< E >_{exp}$[a]	$< E >_{th}$[b]
mP(10N)$_2$	0.97	0.90	0.67	0.94	0.94
FemP(10N)$_2$ (CH_3OH)	0.97	0.92	0.66	0.95	0.95
FemP(10N)$_2$ H_2O/CH_3OH (9 : 1)$_{v/v}$, pH = 7.5	0.97	0.90	≈0	0.93	0.96

[a] From the data reported in Table 2.
[b] From molecular mechanics calculations.

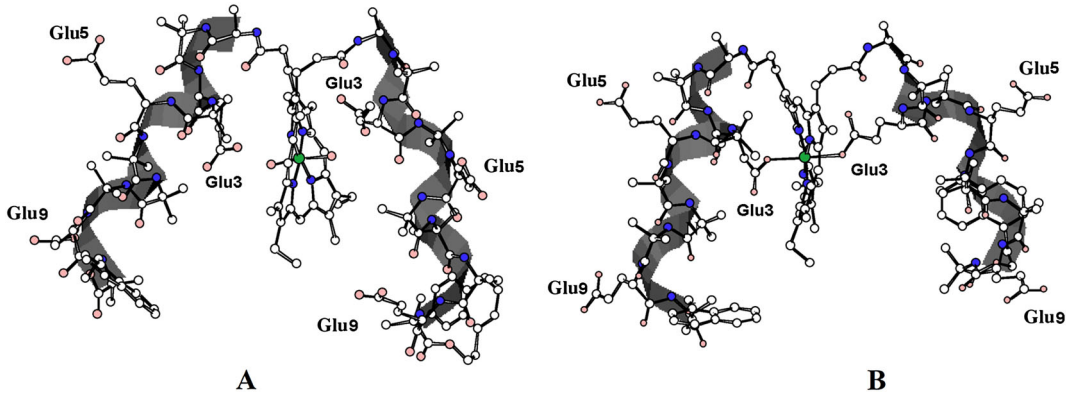

Figure 7. Most populated conformer of FemP(10N)$_2$ in H_2O/CH_3OH (9 : 1)$_{v/v}$ at pH = 4 (A) and at pH 7.5 (B) from molecular mechanics calculations. C atoms: white circles; N: blue circles; O: red circles; Fe: green circle. Hydrogen atoms were omitted for clarity. The helical arrangement of the peptide backbone was schematized by a ribbon representation.

center in Fe–His or Fe–imidazole adducts [2]. This finding is in good agreement with the UV–vis absorption spectrum of FemP(10N)$_2$, typical of a high-spin Fe(III) system. As clearly shown in Figure 7B, the Fe(III)–O(Glu3) interaction constrains the peptide segment in the proximity of the porphyrin active site, leaving however to the oxidant the possibility to approach the porphyrin ring and compete with the carboxylate group for Fe(III) coordination. As expected, the other Glu residues are positioned at the outer surface of the peptide helices, completely exposed to the solvent molecules.

From the calculated structures, an average theoretical quenching efficiency can be obtained by summing over the quenching efficiencies associated to each of the significantly populated conformers:

$$< E >_{th} = \sum_j w_j \sum_{i=1}^{2} E_i \qquad (8)$$

where w_j is the Boltzmann weight associated to the j-th conformer, as given by

$$w_j = \frac{\exp(-U_j/RT)}{\sum_j(\exp - U_j/RT)} \qquad (9)$$

and E_i is the efficiency associated to each of the two naphthyl–FemP FRET pairs in the j-th conformer, characterized by a potential energy U_j. The calculated average quenching efficiency $< E >_{th}$ can be directly compared with the experimental average quenching efficiency $< E >_{exp}$ (Table 3). The fine agreement between experimental and calculated parameters makes reasonable to consider the computed structures a good representation of the conformations actually populating the solution.

It should be noted that the large R_0 value of the naphthyl–FemP D–A pair makes the experimental quenching efficiencies not very sensitive to the naphthyl–FemP distance. However, when the Glu3–Fe interaction is relaxed and the peptides forced to dip straight into the solvent in extended conformation, so that the catalyst attains a totally 'open' structure, the naphthyl–FemP center-to-center distance increases to ~30 Å. In this case, the calculated FRET quenching efficiencies take values ranging from 0.6 to 0.8, definitely smaller than the experimental data. Taken together, the results of conformational analysis and FRET experiments indicate that FemP(10N)$_2$ at pH 7.5 attains a rather compact 3D structure, the access to the active site being somewhat restricted by the folding of the peptide chains. The Fe(III) porphyrin moiety appears to be more protected against a direct attack of oxidants and the peptide chains more rigidly held in the proximity of the active site. For this reason, all kinetic experiments were carried out at pH 7.5.

Kinetic and Conformational Studies on the Catalytic Activity of FemP(N10)$_2$

Kinetic results

The catalytic activity of FemP(10N)$_2$ has been investigated in the oxidation of L- and D-Dopa by H_2O_2 in a H_2O/CH_3OH (9 : 1)$_{v/v}$ solution at pH = 7.5 (T = 25 °C). The iron-catalyzed oxidation of L- and D-Dopa is a well-known reaction, and it is here addressed as a reference reaction to assess the catalytic properties of FemP(10N)$_2$ (Scheme 1) [28].

Detailed mechanistic studies on the peroxidase-catalyzed oxidation of Dopa revealed the formation of two active intermediates, often referred as Cpd I ($^+$E-Fe^{IV}=O) and Cpd II ($^+$EH-Fe^{IV}=O) [29,30]. A third low-reactive intermediate was found to be responsible for inactivation of peroxidase [31]. Recent literature also reported on the formation of phenoxy radicals during the oxidation of L-Dopa in the presence of horseradish peroxidase followed by radical dismutation [32]. Despite the complexity of the mechanism, a Michaelis–Menten approach has been generally found most appropriate to describe enzymatic oxidation of Dopa substrates [33,34]. The formation of dopaquinone, an intermediate product in the Dopa oxidation pathway, can be easily monitored by UV–vis absorption spectroscopy [35,36]. Final oxidation products of the reaction are dopachrome and, after polymerization, melanine [37].

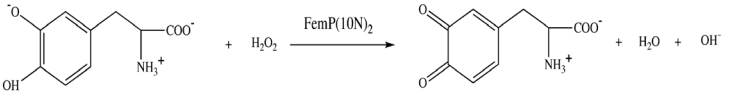

Scheme 1. Oxidation of Dopa by hydrogen peroxide in the presence of FemP(10N)$_2$ catalyst.

Journal of PeptideScience

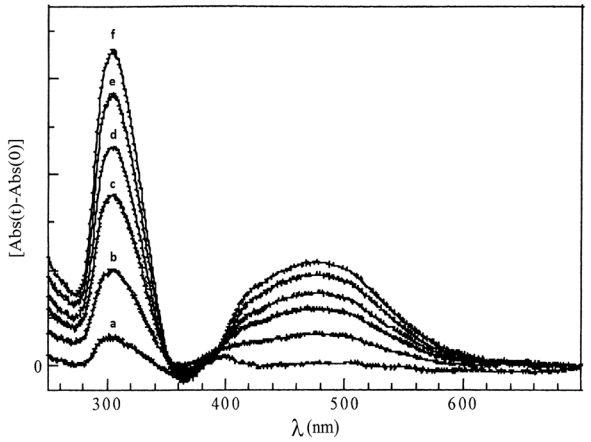

Figure 8. Absorption spectra of the L-Dopa/FemP(10N)$_2$ solution at increasing time intervals: (a) 3 min, (b) 9 min, (c) 20 min, (d) 28 min, (e) 40 min, and (f) 50 min from the addition of H_2O_2 ($t = 0$). The reported spectra were subtracted by the spectrum at $t = 0$.

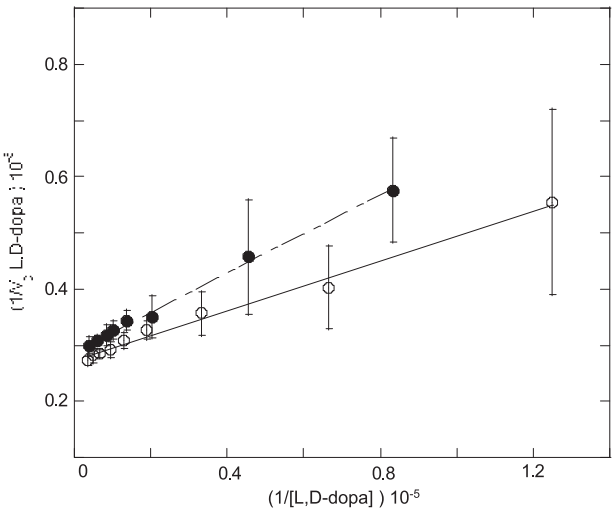

Figure 9. Double reciprocal plot of initial velocity *versus* concentration for the oxidation reaction of L- (○) and D-Dopa (●) by H_2O_2 in the presence of the FemP(10N)$_2$ catalyst.

The time evolution of the absorption spectrum of an L-Dopa solution when reacted with H_2O_2 at micromolar concentration of FemP(10N)$_2$ is reported in Figure 8 (actually, the reported spectra were subtracted by the spectrum at $t = 0$). The formation of dopaquinone can be clearly observed at $\lambda_{max} = 304$ and 475 nm. Most importantly, the Soret absorption at $\lambda_{max} = 393$ nm did not show any perturbation, indicating that the catalyst was not degraded in the course of the reaction. This result was confirmed by studying the stability of FemP(10N)$_2$ in the presence of increasing concentrations of H_2O_2. For a FemP(10N)$_2$: H_2O_2 1 : 10 solution and in absence of the substrate molecule, the observed catalyst degradation after 30 min was only 9%. This finding indicates that the peptide environment shielded effectively the FemP active site from unwanted side reactions and degradation processes, still allowing for the catalyst–oxidant interaction leading to the formation of the Fe-oxo reactive intermediates. Control measurements carried out on a Dopa/H_2O_2 solution in the absence of the catalyst did not reveal the formation of dopaquinone in detectable amount.

The stereoselective properties of FemP(10N)$_2$ were investigated by comparing the oxidation kinetics of L- and D-Dopa by H_2O_2, following the time dependence of the dopaquinone absorption at $\lambda = 310$ nm. The kinetic curves showed a typical saturation trend, suggesting that a simple Michaelis–Menten treatment can be successfully applied.

The double reciprocal plot of the initial velocity *versus* L- or D-Dopa substrate concentration at a fixed micromolar catalyst concentration is shown in Figure 9. The kinetic parameters of the reaction, that is, the catalytic (k_{cat}) and Michaelis–Menten (K_M) constants, obtained by the reported experimental data, are listed in Table 4. Very similar catalytic rate constants were obtained for the oxidation of the L- and D-Dopa enantiomers, suggesting poor stereoselective properties of the FemP(10N)$_2$ catalyst. However, the Michaelis–Menten constants differ by more than 30%, suggesting a significant major affinity of L-Dopa for the catalyst. As a result, the ratio between the catalytic and Michaelis–Menten constants, that is, k_{cat}/K_M, is 5.31 10^5 M^{-1} s^{-1} and 3.35 10^5 M^{-1} s^{-1} for the L- and D-Dopa, respectively, denoting weak but not negligible stereoselective properties [38]:

$$\frac{k_{cat}(\text{L-Dopa})}{k_{cat}(\text{D-Dopa})} \times \frac{k_M(\text{D-Dopa})}{k_M(\text{L-Dopa})} = 1.6 \pm 0.3$$

Table 4. Kinetic parameters for the oxidation of L- and D-Dopa by H_2O_2 catalyzed by FemP(10N)$_2$

k_{cat}/s^{-1}	$10^{-5} \cdot K_M/M$	10^5 k_{cat}/K_M
6.8 ± 0.2	1.28 ± 0.05	5.31
6.2 ± 0.2	1.85 ± 0.05	3.35

Conformational analysis of the (L,D)Dopa–catalyst adducts

The formation of L- and D-Dopa adducts with the new FemP(10N)$_2$ catalyst was investigated by molecular mechanics calculations. In particular, the approach of the substrate to the active site was analyzed along 100 different trajectories, starting from initial positions equally distributed on a spherical surface having a 15 Å radius and centered on the Fe(III) ion, and searching for the minimum energy structure of the L- and D-Dopa/FemP(10N)$_2$ adducts. The obtained minimum energy structures in H_2O/CH_3OH $(9:1)_{v/v}$ at pH = 7.5 are reported in Figure 10A and 10B for the L- and D-Dopa adducts with FemP(10N)$_2$, respectively. It was found that both L- and D-Dopa can reach the active site, approaching the periphery of the porphyrin ring through its catecholic group. UV–vis measurements confirmed the weak character of the catalyst–substrate interaction, the Soret transition remaining unperturbed by the formation of the L- or D-Dopa/FemP(10N)$_2$ adducts. By taking into account the most populated computed structures, the energetic binding of the L- and D-Dopa with FemP(10N)$_2$ results from a complex interplay of electrostatic and weak interactions that ultimately leads to a modest difference in the stability of the two adducts, slightly favoring the L-Dopa/FemP(10N)$_2$ encounter complex [ΔU(L-Dopa/FemP(10N)$_2$) – ΔU(D-Dopa/FemP(10N)$_2$) = −0.9 kcal mol^{-1}]. This result qualitatively confirms the experimental finding of a lower Michaelis–Menten constant for the L-Dopa/FemP(10N)$_2$ adduct.

From the structures reported in Figure 10, it can be noted that (i) the penetration of L-Dopa into the catalyst sphere of action causes the partial displacement of the Glu3 residue involved in the coordination of Fe(III) and (ii) for both L- and D-Dopa, the approach to the FemP active site takes place through its catecholic oxygen, relatively far from the chiral groups

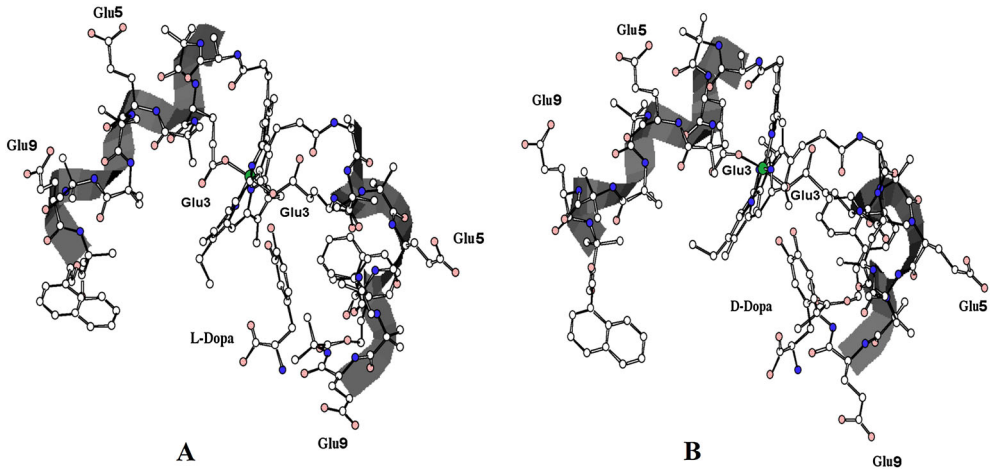

Figure 10. Minimum energy structure of the L-Dopa (A) and D-Dopa (B) adduct with FemP(10N)$_2$ in H_2O/CH_3OH $(9:1)_{v/v}$ at pH 7.5 from molecular mechanics calculations. C atoms: white circles; N: blue circles; O: red circles; Fe: green circle. Hydrogen atoms were omitted for clarity. The helical arrangement of the peptide backbone was schematized by a ribbon representation.

discriminating between the L and D enantiomers. This finding clearly explains for the observed moderate stereoselectivity of the FemP(10N)$_2$ catalyst.

Conclusions

The structural features of a *de novo* designed catalyst based on a Fe(III)-mesoporphyrin IX group covalently linked to two helical decapeptides were investigated by spectroscopic techniques (CD, FTIR, NMR, UV–vis, steady-state, and time-resolved fluorescence) and theoretical conformational analysis. The most stable structure in CH_3OH was obtained when the peptide chains attain an α-helical conformation, experiencing only a weak interaction with the heme group. On the other hand, in H_2O/CH_3OH $(9:1)_{v/v}$ at pH 7.5, the synthetic mini-enzyme attains a more compact 3D structure, characterized by the coordination of one or, possibly, two Glu carboxylate groups to the Fe(III) central ion. This coordination is promoted by an $\alpha\text{-}\rightarrow 3_{10}$-helix conformational transition of the two peptide chains, giving rise to a sterically hindered chiral environment, protecting the active site. This effect is particularly relevant in the absence of Hys residues in the iron-porphyrin coordination shell and represents the most important element of novelty of this work.

The catalytic properties of FemP(10N)$_2$ were investigated with respect to the oxidation of L- and D-Dopa by hydrogen peroxide. The synthesized catalyst effectively speeds up the reaction, showing optimal resistance against degradation under the experimental conditions used. Kinetic studies revealed that the catalyzed reaction can be satisfactorily described by a simple Michaelis–Menten mechanism. Although the stereoselective properties of the new catalyst were found to be of moderate relevance when considered in absolute terms, they are encouraging in comparison with the enantiomeric discrimination capacity of low molecular weight analogs. These effects principally originate from the rigid helical structure and the conformationally constrained character of the two decapeptide chains, determined by the high content of C^{α}-tetrasubstituted residues (Aib). Molecular mechanics calculations showed that the approach of both L- and D-Dopa to the FemP active site occurs through the catecholic oxygen of Dopa, which limits the influence of the chiral region of the substrate on the reaction.

This contribution emphasizes the importance to control the conformational properties of biomimetic synthetic catalysts for determining the efficiency and the stereochemical preference of the catalyzed reaction.

Acknowledgements

The kind hospitality of the Laboratory of Peptide Synthesis headed by Prof. Claudio Toniolo (University of Padova, Italy) is gratefully acknowledged. We thank Prof. Basilio Pispisa (University of Rome Tor Vergata) for stimulating discussion and critical reading of the paper. This research was funded by the Italian Minister for University and Research (MIUR), PRIN 2010–2011 No. 2010FM738P.

References

1 *Metalloporphyrins in Catalytic Oxidations*, Sheldon RA (ed.). Marcel Dekker: New York, 1994.
2 Loew GH, Harris DL. Role of the heme active site and protein environment in structure, spectra, and function of the cytochrome P450s. *Chem. Rev.* 2000; **100**: 407–419; Meunier B, de Visser SP, Shaik S. Mechanism of oxidation reactions catalyzed by cytochrome P450 enzymes. *Chem. Rev.* 2004; **104**: 3947–3980.
3 Woggon W-D Metalloporphyrins as active site analogues – lessons from enzyme and enzyme models. *Acc. Chem. Res.* 2005; **38**: 127–136; Shaik S, Kumar D, de Visser AP, Altun A, Thiel W. Theoretical perspective on the structure and mechanism of cytochrome P450 enzymes. *Chem. Rev.* 2005, **105**: 2279–2328.
4 Lombardi A, Nastri F, Pavone V. Peptide-based heme-protein models. *Chem. Rev.* 2001; **101**: 3165–3189; Reedy CJ, Gibney BR. Heme-protein assemblies. *Chem. Rev.* 2004; **104**: 617–649; Nicolis S, Casella L, Roncone R, Dallacosta C, Monzani E. Heme-peptide complexes as peroxidase models. *C.R. Chimie* 2007; **10**: 380–391.
5 Low DW, Yang G, Winkler JR, Gray JB. Modification of heme peptides by reverse proteolysis: spectroscopy of microperoxidases-10 with C-terminal histidine, tyrosine and methionine residues. *J. Am. Chem. Soc.* 1997; **119**: 4094–4095.
6 Casella L, Monzani E, Fantucci P, Gullotti M, De Gioia L, Strini A, Chillemi F. Axial imidazole distortion effects on the catalytic and binding properties of chelated deuterohemin complexes. *Inorg. Chem.* 1996; **35**: 439–444; Monzani E, Linati L, Casella L, De Gioia L, Favretto M, Gullotti M, Chillemi F. Synthesis, characterization and stereoselective catalytic oxidations of chelated deuterohaemin-glycyl-L-histidine complexes. *Inorg. Chim. Acta* 1998; **273**: 339–345; Franceschi F, Gullotti M, Monzani E, Casella L, Papaefthymiou V. Cytochrome C oxidase models. A novel dinuclear iron-copper complex derived from a covalently modified deuteroporphyrin-L-histidine-bis(benzimidazole) ligand. *Chem. Commun.* 1996; 1645–1646.

7 Choma CT, Lear JD, Nelson MJ, Dutton PL, Robertson DE, DeGrado WF. Design of a heme-binding four-helix bundle. *J. Am. Chem. Soc.* 1994; **116**: 856–865.
8 Broo KS, Nilsson H, Nilsson J, Baltzer L. Substrate recognition and saturation kinetics in *de novo* designed histidine-based four-helix bundle catalysts. *J. Am. Chem. Soc.* 1998; **120**: 10287–10295.
9 Aili D, Enander K, Baltzer L, Liedberg B. Synthetic *de novo* designed polypeptides for control of nanoparticle assembly and biosensing. *Biochem. Soc. Trans.* 2007; **35**: 532–534.
10 Ye S, Discher BM, Strzalka J, Xu T, Wu SP, Noy D, Kuzmenko I, Gog T, Therien MJ, Dutton PL, Blasie JK. Amphiphilic four-helix bundle peptides design for light-induced electron transfer across a soft interface. *Nano Lett.* 2005; **5**: 1658–1667.
11 Nastri F, Lombardi A, Morelli G, Maglio O, D'Auria G, Pedone C, Pavone V. Hemoprotein models based on a covalent helix-heme-helix sandwich: 1. Design, synthesis and characterization. *Chem. Eur. J.* 1997; **3**: 340–349; D'Auria G, Maglio O, Nastri F, Lombardi A, Mazzeo M, Morelli G, Paolillo L, Pedone C, Pavone V. Hemoprotein models based on a covalent helix-heme-helix sandwich: 2. Structural characterization of Co(III) mimochrome I δ and λ isomers. *Chem. Eur. J.* 1997; **3**: 350–362; Lombardi A, Nastri F, Marasco D, Maglio O, De Sanctis G, Sinibaldi F, Santucci R, Coletta M, Pavone V. Design of a new mimochrome with unique topology. *Chem. Eur. J.* 2003; **9**: 5643–5654.
12 Benson DR, Hart BR, Zhu X, Dougthy MB. Design, synthesis and circular dichroism investigation of a peptide sandwiched mesoheme. *J. Am. Chem. Soc.* 1995; **117**: 8502–8510; Arnold PA, Benson DR, Brink DJ, Hendrich MP, Jas GS, Kennedy ML, Petasis DT, Wang M. Helix induction and springboard strain in peptide-sandwiched mesohemes. *Inorg. Chem.* 1997; **36**: 5306–5315; Wang M, Kennedy ML, Hart BR, Benson DR. The bis-p-nitrophenyl ester of iron(III) mesoporphyrin II acetate: preparation and incorporation into a model protein. *Chem. Commun.* 1997; 883–884; Williamson DA, Benson DR. Remarkable helix stabilization via edge-to-face tryptophan-porphyrin interaction in a peptide-sandwiched mesoheme. *Chem. Commun.* 1998; 961–962; Liu D, Williamson DA, Kennedy ML, Williams TD, Morton MM, Benson DR. Aromatic side chain-porphyrin interactions in designed hemoproteins. *J. Am. Chem. Soc.* 1999; **121**: 11798–11812.
13 Toniolo C, Crisma M, Formaggio F, Peggion C. Control of peptide conformation by the Thorpe-Ingold effect (C^{α}-tetrasubstitution). *Biopolymers (Pept. Sci.)* 2001; **60**: 396–415.
14 Pispisa B, Palleschi A, Mazzuca C, Stella L, Valeri A, Venanzi M, Formaggio F, Toniolo C, Broxterman QB. The versatility of combining FRET measurements and molecular mechanics results for determining the structural features of ordered peptides in solution. *J. Fluoresc.* 2002; **12**: 213–217.
15 Guallar V. Heme electron transfer in peroxidases: the propionate e-pathway. *J. Phys. Chem. B* 2008; **112**: 13460–13464.
16 Pispisa B, Stella L, Venanzi M, Palleschi A, Viappiani C, Polese A, Formaggio F, Toniolo C. Quenching mechanisms in bichromophoric 3_{10}-helical Aib-based peptides, modulated by chain length dependent topologies. *Macromolecules* 2000; **33**: 906–915.
17 Pispisa B, Venanzi M, Stella L, Palleschi A, Zanotti G. Photophysical and structural features of covalently bound peptide-protoporphyrin-peptide compounds carrying naphthalene chromophores. *J. Phys. Chem. B* 1999; **103**: 8172–8179.
18 Allinger NL, Chen K, Lii J-H. An improved force field (MM4) for saturated hydrocarbons. *J. Comp. Chem.* 1996; **17**, 642–668; Nevens N, Chen K, Allinger K. Molecular mechanics (MM4) calculations on alkenes. *J. Comp. Chem.* 1996; **17**, 669–694; Nevins N, Lii J-H, Allinger NL. Molecular mechanics (MM4) calculations on conjugated hydrocarbons. *J. Comp. Chem.* 1996; **17**, 695–729; Nevins N, Allinger NL. Molecular mechanics (MM4) vibrational frequency calculations for alkenes and conjugated hydrocarbons. *J. Comp. Chem.* 1996; **17**, 730–746.
19 Pispisa B, Palleschi A, Stella L, Venanzi M, Mazzuca C, Formaggio F, Toniolo C, Broxterman QB. Effects of helical distortions on the optical properties of amide NH infrared absorption in short peptides in solution. *J. Phys. Chem. B* 2002; **106**: 5733–5738.
20 Polese A, Formaggio F, Crisma M, Valle G, Toniolo C, Bonora GM, Broxterman QB, Kamphuis J. Peptide helices as rigid molecular rulers: a conformational study of isotactic homopeptides from α-methyl-α-isopropylglycine, [L-(αMe)Val]$_n$. *Chem. Eur. J.* 1996; **2**: 1104–1111.
21 Toniolo C, Polese A, Formaggio F, Crisma M, Kamphuis J. Circular dichroism spectrum of a peptide 310-helix. *J. Am. Chem. Soc.* 1996; **118**: 2744–2745.
22 Toniolo C, Formaggio F, Tognon S, Broxterman QB, Kaptein B, Huang R, Setnicka V, Keiderling TA, McColl IH, Hecht L, Barron LD. The complete chirospectroscopic signature of the peptide 3_{10}-helix in aqueous solution. *Biopolymers* 2004; **75**: 32–45.
23 Eaton WA, Hofrichter J. Polarized absorption and linear dichroism spectroscopy of hemoglobin. *Methods Enzymol.* 1981; **76**: 175–261.
24 Pispisa B, Palleschi A, Venanzi M, Zanotti G. Conformational statistics and energetic analysis of sequential peptides undergoing intramolecular transfer of excitation energy. *J. Phys. Chem.* 1996; **100**: 6835–6844.
25 Toniolo C, Formaggio F, Crisma M, Mazaylerat J-P, Wakselman M, George C, Deschamps JR, Flippen-Anderson JL, Pispisa B, Venanzi M, Palleschi A. First peptide-based system of rigid donor-rigid interchromophore spacer-rigid acceptor: a structural and photophysical study. *Chem. Eur. J.* 1999; **5**: 2254–2264.
26 Venanzi M, Gatto E, Bocchinfuso G, Palleschi A, Stella L, Baldini C, Formaggio F, Toniolo C. Peptide folding dynamics: a time-resolved study from the nanosecond to the microsecond time regime. *J. Phys. Chem. B* 2006; **110**: 22834–22841.
27 Pispisa B, Palleschi A, Stella L, Venanzi M, Toniolo C. A nitroxide derivative as a probe for conformational studies of short linear peptides in solution. A spectroscopic and molecular mechanics investigation. *J. Phys. Chem. B* 1998; **102**: 7890–7898.
28 Pispisa B. In *The Coordination Chemistry of Metalloporphyrins*, Bertini I, Drago RS, Luchinat C (eds). D. Reidel Publ. Co.: Dordrecht, The Netherlands, 1983; 279–290.
29 Dunford HB. *Heme Peroxidases*. Wiley-VCH: New York, 1999.
30 Sanchez Ferrer A, Rodriguez-Lopez JN, Garcia-Canovas F, Garcia-Carmona F. Tyrosinase: a comprehensive review of its mechanism. *Biochim. Biophys. Acta, Protein Struct. Mol. Enzymol.* 1995; **1247**: 1–11.
31 Adedrain S, Lambeir AM. Kinetics of the reaction of compound II of horseradish peroxidase with hydrogen peroxide to form compound III. *Eur. J. Biochem.* 1989; **186**: 571–576.
32 Munoz-Munoz JL, Garcia-Molina F, Varon R, Tudela J, Garcia-Canovas F, Rodrigues-Lopez JN. Generation of hydrogen peroxide in the melanin biosynthesis pathway. *Biochim. Biophys. Acta* 2009; **1794**: 1017–1029.
33 Adams PA, de L Milton RC, Byfield MP, Pratt JM. Oxygen activation and ligand binding by pure heme-octapeptide microperoxidase-8 (MP-8). *J. Inorg. Biochem.* 1988; **34**: 167–175.
34 Kubo I, Chen Q-X, Nihei KI, Calderon JS, Cespedes CL. Tyrosinase inhibitors from galls of *Rhus javanica* leaves and their effects on insects. *Z. Naturforsch.* 2003; **58c**: 703–718.
35 Martin RB. Zwitterion formation upon deprotonation in L-3,4-dihydroxyphenylalanine and other phenolic amines. *J. Phys. Chem.* 1971; **75**: 2657–2661.
36 Barteri M, Pispisa B. Stereospecific oxidation of ascorbic acid by chiral association complexes between polypeptides and iron(III) chelate ions. *Biopolymers* 1982; **21**: 1093–1106.
37 In *Bioinorganic Catalysis*, Reedijk J (ed.). Marcel Dekker: New York, 1993.
38 In *Metalloporphyrins Catalyzed Oxidation*, Montanari F, Casella L, Kluwer Academic Publ.: Dordrecht, The Netherlands, 1994.

Supporting Information

Additional supporting information may be found in the online version of this article at the publisher's web site.

